

1
2
3
4
5
6
7
8
9
10
11
12
13
14
15

Mechanical Properties of the Rocky Interiors of Icy Moons

Cassandra Seltzer¹, Hoagy O. Ghaffari¹, Matěj Peč¹

¹Massachusetts Institute of Technology, Department of Earth, Atmospheric, and Planetary Sciences, Massachusetts, USA

Corresponding author: Cassandra Seltzer (cseltz@mit.edu)

Key points:

1. We established the failure envelope of chondritic materials under conditions relevant to the rocky interiors of small icy moons
2. Chondritic material has a yield cap around 50 MPa confining pressure, above which its porosity is very small
3. Pressurization and deformation of chondritic material creates energetic cracks, which could contribute to heat dissipation

16

17 Abstract

18 Icy moons in the outer Solar System contain rocky, chondritic interiors, but this material is rarely studied
19 under confining pressure. The contribution of rocky interiors to deformation and heat generation is
20 therefore poorly constrained. We deformed LL6 chondrites at confining pressures ≤ 100 MPa and
21 quasistatic strain rates, and recorded acoustic emissions (AEs) using ultrasound probes. We defined a
22 failure envelope, measured ultrasonic velocities, and retrieved elastic moduli for the experimental
23 conditions. Chondritic material stiffened with increasing confining pressure, and reached its peak
24 strength at 50 MPa confining pressure. Microcracking events occurred at low stresses, during nominally
25 “elastic” deformation, indicating that dissipative processes are possible in rocky interiors. These events
26 were most energetic at lower differential stresses, and occurred more frequently at lower confining
27 pressures. We suggest that chondritic interiors of icy moons are therefore stronger, less compliant, and
28 less dissipative with increasing pressure and size.

29

30 Plain language summary

31 Many icy moons in the outer Solar System have warm, active interiors, but the source of the heat that
32 maintains this activity is sometimes unknown. Many of these moons contain rocky layers which are made
33 of the same material as meteorites that have landed on the Earth. However, we have never previously
34 studied how this material deforms under confining pressures like those found within icy moons. We
35 conducted a lab study of the deformation mechanisms of meteoritic material to study how the deformation
36 response applies to the interior of icy moons. We also analyzed cracking in response to small stress
37 changes, which occurred at all stages of deformation. We found that the material behaved differently at
38 low and high confining pressures, with a peak strength at ~ 50 MPa. This indicates that icy moons with
39 smaller oceans and thinner crusts may deform differently than larger icy moons, and can receive some of
40 the heat needed to maintain their oceans through cracking processes in their porous cores.

41

42

43

44 1. Introduction

45 Icy moons in the outer Solar System are considered excellent candidate bodies for hosting extraterrestrial
46 life. The interior properties of these moons are important for determining the feasibility of life, lander
47 missions, and future priorities in exploring the outer Solar System. The mechanical properties of the cores
48 of these moons are relatively less well-studied than the properties of their icy crusts and water oceans, as
49 the cores are likely less dissipative than the ice or liquid layers (e.g., Tobie et al., 2005). The deformation
50 mechanisms of core material are thus presently still unknown, leaving large uncertainties as to how
51 dissipation proceeds throughout the entire body: there is an order-of-magnitude difference in potential
52 heat release from Enceladus’ core, for example, depending on if it is stiff and elastic or if it is highly
53 deformable and (poro)viscoelastic (Aygün and Čadek, 2022; Rovira-Navarro et al., 2022).

54 The yield strength of a material, which modelers use to predict how a body responds to stress, is
55 almost always pressure-dependent, and often strain-rate dependent (Mair et al., 2002; Mulliken and
56 Boyce, 2006). Rocky components of icy moons are frequently chondritic in nature (Kuskov and Kronrod,
57 2005; Néri et al., 2020; Neumann and Kruse, 2019), and most strength tests of meteoritic material are
58 conducted at asteroidal conditions: no confinement, and fast strain rates.

59 Confining pressures at the core-ocean or core-mantle boundary of icy moons frequently reach tens of
60 MPa and more (Neveu et al., 2015; Styczinski et al., 2022; Vance et al., 2018). Almost all tests on
61 meteoritic material occur at room pressure (Pohl and Britt, 2020). The few tests that do assess strength
62 and deformation mechanisms of chondritic material under pressure (Ramesh et al., 2017; Voropaev et al.,
63 2017) do not report strength at pressures relevant to rocky interiors of icy moons. Voropaev et al. (2020)
64 did study a single sample at confining pressure of 50 MPa, but did not apply any differential stress and
65 therefore could not measure the strength of the material. Dynamic (fast) deformation experiments
66 simulating crater formation and impacts on chondrites are also common. These experiments are not easily
67 applied to planetary strain rates, and there is a larger rate sensitivity in unconfined meteoritic material
68 than in terrestrial rocks (Kimberley and Ramesh, 2011). Hogan et al. (2015) used Brazilian disk tests in a
69 Kolsky bar apparatus under confined planar configuration at dynamic strain rates of $10^1 - 10^3 \text{ s}^{-1}$, which
70 yielded a higher peak strength (~ 300 MPa) than the unconfined tests at similar strain rates, but did not
71 record enough data at low strain rates to establish a definite change in peak strength for quasistatic tests
72 conducted at no confining pressure vs. those conducted under confinement.

73 Here, we report the mechanical properties of deforming chondritic material under confining pressure.
74 These measurements represent the first experimental investigation of chondritic material deformation
75 under confining pressure similar to that found inside an icy moon. We used fallen meteoritic material,
76 which is inherently pre-deformed and high-strength. These fallen meteorites are analogs for the rocky
77 cores and mantles of moons, which have survived accretion and continuous tidal deformation for billions
78 of years (Nimmo and Pappalardo, 2016).

79 In addition to the bulk mechanical response to deformation, we also studied microcracking behavior as
80 the rocks were pressurized, and subsequently deformed at elevated confining pressures. Cracks associated
81 with damage emit dynamic stress waves, observable as acoustic emissions (AEs) with characteristic
82 frequencies depending on the source characteristics of deformation (Eitzen and Wadley, 1984; Ghaffari et
83 al., 2014; Lei and Ma, 2014; Li et al., 2021; O’Ghaffari et al., 2023). The internal structure can also be
84 sampled using throughgoing waves, which acquire signatures of the microstructure as they propagate
85 through and interact with the material. We used ultrasonic probes in passive and active modes to measure
86 1) energy release associated with acoustic emissions, and 2) variations of sound velocities and their
87 transmissivity in the samples under confining pressure. As macroscale behavior arises from microscale
88 effects, data from all scales is needed to produce a robust picture of deformation dynamics.

89 This paper presents mechanical results from deformation tests, followed by observations of internal
90 structure based on acoustic emissions and ultrasonic pulsing. We show that as the meteoritic material
91 encounters higher confining pressures up to 50 MPa, the samples become stronger and emitted high-energy
92 acoustic waves. Above 50 MPa confining pressure, the material became weaker, and dissipated less energy
93 via AEs. Our observations indicate that the mechanisms of deformation are controlled by porosity closure,
94 and that the dissipation of stored energy via microcracking is more pronounced at lower confining
95 pressures.

96

97 **2. Methods**

98 These tests were conducted on samples from the Kilabo meteorite, an LL6 chondrite. Moons have
 99 broadly chondritic silicate interiors: Néri et al. (2020) suggest that the cores of Titan and Ganymede (and
 100 possibly Callisto) are carbonaceous chondrites, while Kuskov and Kronrod (2005) infer a low metallicity
 101 and/or low iron (L/LL) composition for the interior of Europa (and, again, possibly Callisto), and
 102 Neumann and Kruse (2019) find an ordinary chondritic (OC) composition (likely L/LL) for the rocky
 103 core of Enceladus. Previous experiments suggest that strength differences between carbonaceous and
 104 ordinary chondrites are related to the higher porosity of carbonaceous chondrites rather than any inherent
 105 difference in the material (Flynn et al., 2018; Pohl and Britt, 2020).

106 The meteoritic material was impregnated in epoxy before being drilled into 6.25 mm diameter cores for
 107 laboratory deformation. The samples were jacketed in soft PVC tubing, then encased in Teflon heat
 108 shrink tubing prior to deformation (Supplementary material). This material has ~15% microporosity and a
 109 mean density of ~2.5 g/cm³. However, these (and other) properties are heterogeneously distributed
 110 throughout the sample. Samples were taken from the interior of the meteorite, and there is no alteration
 111 crust present. Deformation was performed in a Paterson gas medium deformation apparatus (Paterson,
 112 1990) housed in the Rock Mechanics Laboratory at MIT. A summary of the experimental parameters can
 113 be found in Supplemental Table 1, and a setup schematic can be found in Figure S1.

114 We applied isostatic confining pressures (σ_3) of up to 100 MPa, and deformed the samples at room
 115 temperature (296 K) and constant strain rates of 10^{-5} s^{-1} , resulting in triaxial stress ($\sigma_1 > \sigma_3 =$
 116 σ_2). Differential stress ($|\sigma_1 - \sigma_3|$) continued to increase until failure, the point at which the samples no
 117 longer supported increasing stress and began to weaken (Figure 2a).

118 A custom data acquisition system (DAQ) was used in order to record passive AEs and pass active
 119 ultrasonic waves through the samples. Miniature piezoelectric sensors with a diameter of 1.5 mm were
 120 created by cementing a piezo-element (0.5 mm tall) within a metallic tube. The piezo-element was then
 121 coated with gold, to achieve high electrical conductivity. These sensors were attached to microsprings and
 122 threaded through pistons to allow constant coupling between the sensor and the sample during
 123 deformation. Signals were amplified at ~60 dB and recorded at 50 MS/s rate with 12 bit resolution using a
 124 digital oscilloscope (TiePie HS4-50). The majority of amplified signals fell in the frequency range of
 125 ~50 kHz to 2 MHz. One of the sensors was set to pulse P-waves (Y-cut LiNbO₃), and the other one
 126 could receive both P and S waves (X-cut).

127 Microcracking occurred during both pressurization and deformation, releasing strain energy and causing
 128 vibrations within the sample. The received signals are recorded as displacements at the end of the sample,
 129 representing a convolution of three main controlling parameters of wave propagation: source
 130 characteristics, the medium through which waves travel, and the sensor response. We took Fourier
 131 Transforms of the displacements u at times t into corresponding frequencies ω , such that $u(\omega) =$
 132 $\sum_t u(t)e^{-i\omega t}$, with amplitudes $\psi_\alpha = \{u(\omega_\alpha)\}$ over frequency levels α . This expansion yields
 133 modulations to the energy state with amplitudes C_α and eigenvectors ϕ_α , which we use to characterize the
 134 state of the system $\vec{\psi}$ such that

$$135 \vec{\psi}(t) = \sum_\alpha C_\alpha e^{-i\omega_\alpha t} \vec{\phi}_\alpha.$$

136

137 For each acoustic emission, we smoothed over the raw emitted waveform with a window of 5 count
138 intervals (0.1 μ s), and denoised using wavelet decomposition. From this data, we computed a spectrogram
139 using the window function W and time index τ to yield power P , such that

$$140 \quad P(\tau, \omega) = \sum_t W(t - \tau) \psi(t) e^{-i\omega t} .$$

141 We integrated over the duration and frequency range of each event to compute the total power, then
142 normalized by the mean power of background noise during each test. The power is a direct indication of
143 how much energy was dissipated due to AEs. We present this quantity as a scalar value relative to the
144 noise threshold, and discarded any events with a power-to-noise ratio below 1.5.

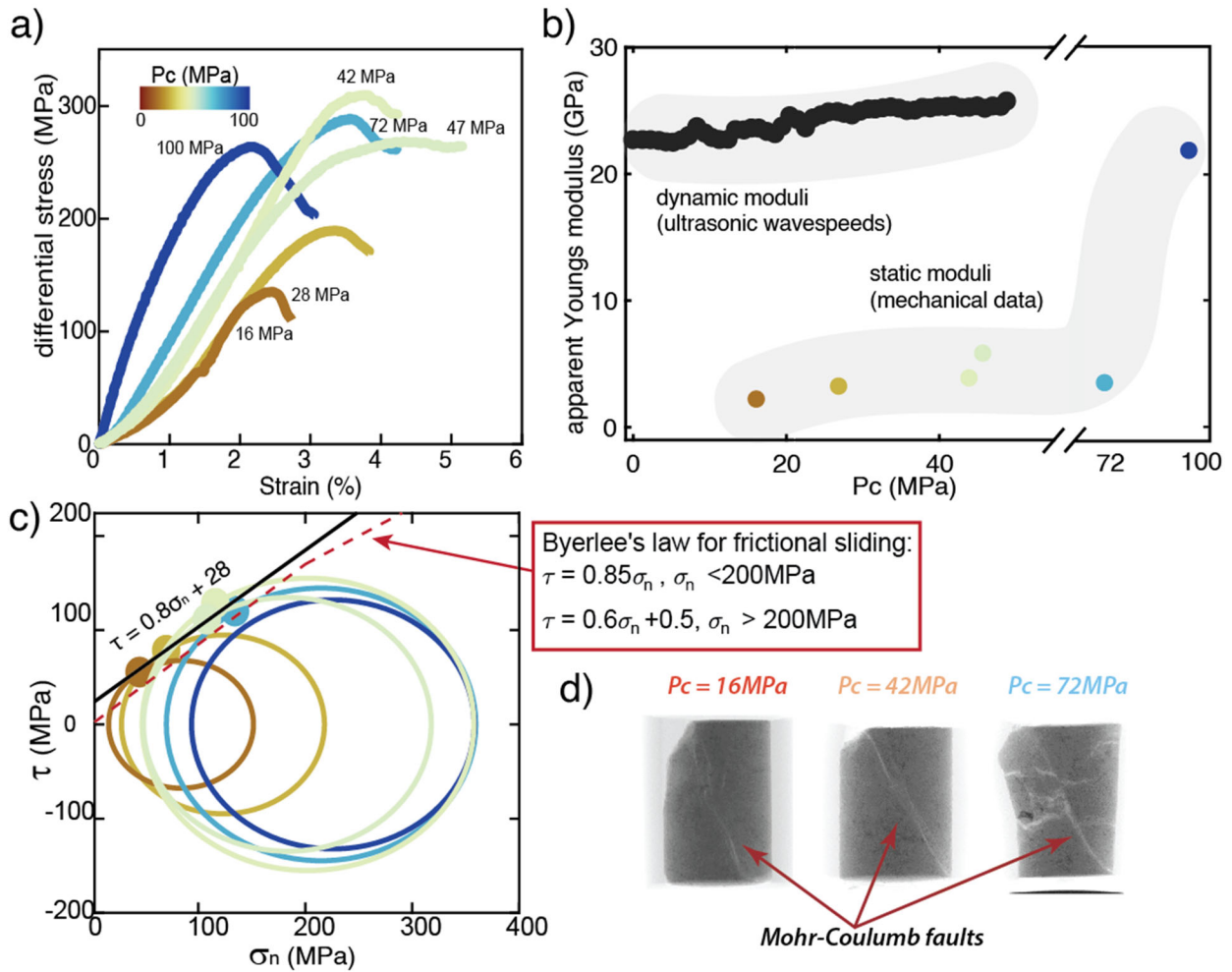
145 See Supplementary Information (figures S2, S3) for more details on acoustic emission data calibration
146 and acquisition. A comprehensive proof of this integration can also be found in the discussion of the P-
147 parameter by Ghaffari et al. (2021).

148 After deformation, entire samples were imaged with the table-top micro-computed tomography (micro-
149 CT) Skyscan system at Woods Hole Oceanographic Institution, using 5-hour scan times at a 4 μ m pixel
150 size under 100 kV acceleration voltage.

151

152

153



154

155 Figure 1: Mechanical results from deformation tests, represented as a) stress/strain curves, colored by
 156 confining pressure, b) observed Young's moduli from ultrasonic and mechanical data, c) Mohr circles,
 157 with a tangent line indicating the Mohr-Coulomb failure envelope, large dots represent fault orientation
 158 developed at failure and d) CT images of deformed samples, with final faults from peak stress indicated.

159 **3. Results**

160 **3.1. Mechanical data**

161 The peak strength of the samples generally increased with confining pressure before reaching a
 162 maximum at ~50 MPa Pc (Figure 1a). Above ~50 MPa confining pressure, peak strength decreased with
 163 increasing confining pressure. The σ_1 did not exceed ~350 MPa in any experiment, and so increases in
 164 confining pressure above 50 MPa lead to decreases in differential stress (Figure 1c). In all cases, the strain
 165 at peak strength at the point of failure remained close to 3%.

166 The failure envelopes of the experimentally deformed samples are represented as Mohr circles in Figure
 167 2c. These Mohr circles are a graphical representation of the stress state within a rock at the point of
 168 failure, plotted in normal stress (σ_n) vs. shear stress (τ) space such that

$$169 \quad \sigma_n = \frac{\sigma_1 + \sigma_3}{2} + \frac{\sigma_1 - \sigma_3}{2} \cos 2\theta ; \tau = \frac{\sigma_1 - \sigma_3}{2} \sin 2\theta ,$$

170

171 where θ is the orientation of the normal to the fault plane with respect to σ_1 . The Mohr-Coulomb failure
172 envelope tangent to the circles indicates the stress conditions expected at failure:

$$173 \quad \tau = 0.8\sigma_n + 28 \text{ (units in MPa).}$$

174 This linear failure envelope is valid only for samples deformed below ~ 50 MPa Pc. Byerlee's Law, which
175 defines the shear stress needed to slide rocks along a pre-existing fault surface, falls below the range of
176 stress states recorded during deformation tests, as expected for the deformation of intact rocks. Notably,
177 no test was able to reach σ_1 greater than 350 MPa; the three highest-pressure tests all failed at this point.

178 During several tests of up to 50 MPa confining pressure, we monitored sound velocities using the
179 piezoelectric sensors placed above and below the sample (See Supplementary Table 1). From these
180 measurements, we characterized dynamic (unrelaxed) Youngs moduli via p- and s-wave arrival times,

$$181 \quad E_{dyn} = \frac{\rho V_s^2 (3V_p^2 - 4V_s^2)}{V_p^2 - V_s^2}.$$

182 We compared the unrelaxed, microscale E_{dyn} with the observed macroscale Youngs modulus derived from
183 mechanical data on stress, σ , and strain, ϵ , such that

$$184 \quad E_{qs} = \frac{\sigma}{\epsilon}.$$

185 As materials are stiffer at higher frequencies and shorter length scales (Jackson, 2015), the calculated
186 Youngs modulus is higher during dynamic probing than during quasistatic bulk deformation (Figure 1b).

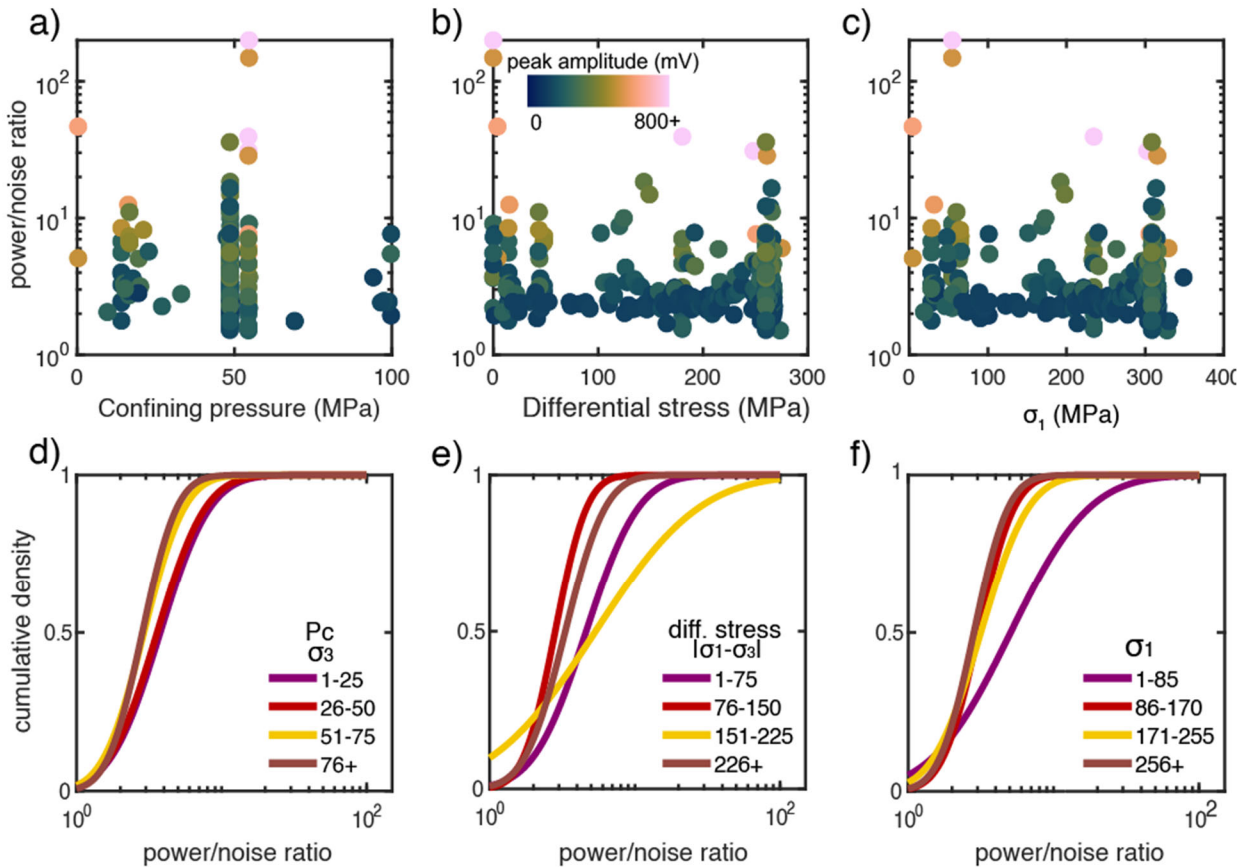
187 **3.2. Ultrasonic probes**

188 **3.2.1. Acoustic emissions**

189 All samples released energy via microcracking, both during pressurization and deformation.
190 Microcracking occurred at all sampled pressures (Figure 2a, 2d). The integrated power and maximum
191 amplitudes of each AEs decreased slightly with increasing differential stress ($|\sigma_1 - \sigma_3|$) (Figure 2b, 2e),
192 and the power-to-noise ratio was largest for low values of σ_1 (Figure 2c, 2f). Many of these energetically
193 dissipative events occurred during the nominally "elastic" deformation period, when differential stress is
194 low and no energy release is expected. The material also emitted energy through microcracking during
195 isotropic pressurization cycles (Figure 3d), when differential stress is zero.

196

197



198

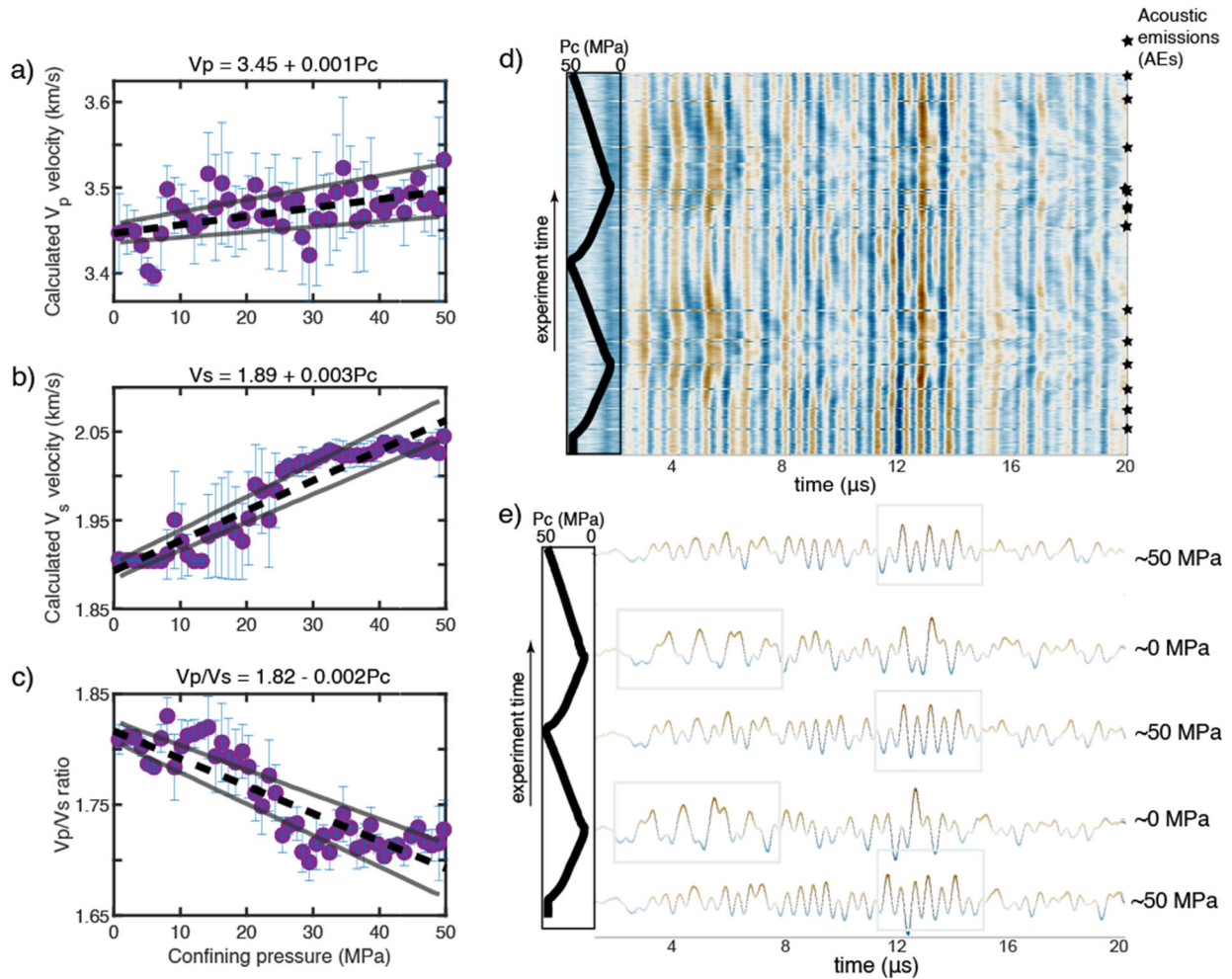
199 Figure 2: (a-c) Power of AEs, normalized by noise threshold for each test, as a function of a) confining
 200 pressure, b) differential stress, c) σ_1 . Each point represents one AE event, and is colored by the maximum
 201 amplitude of that even following the colorbar in panel b). (d-f) Lognormal cumulative distribution
 202 functions of total power per event, evolving as a function of d) confining pressure, e) differential stress,
 203 and f) σ_1 . Colored lines correspond to specific stress ranges, in MPa, which are defined specifically for
 204 each panel in its interior legend.

205

3.2.2. Ultrasonic pulsing

206 To determine wavespeeds as a function of pressure, we sent ultrasonic pulses through a sample
 207 while cycling confining pressure between 0 and 50 MPa, (Figure 3a, 3b, 3c). This procedure allowed us to
 208 examine if pressure oscillations changed the internal structure of our material and validate our results. We
 209 examined the entire waveform to see how the structure is affecting throughgoing waves (Figure 3d, 3e).
 210 The amplitudes and arrival times of throughgoing waves mimicked the pressure conditions, such that at
 211 lower pressures, comparable parts of the waveform arrived later, and at higher pressures, they arrived
 212 earlier (Figure 3d). The waveforms also remained similar at the same pressure even after a
 213 pressurization-depressurization cycle and associated AEs (Figure 3e; S5), suggesting that the
 214 modifications to internal structure of the material occur on smaller length scales than sampled by
 215 ultrasonic waves and therefore would not be visible to seismic waves, regardless of the pressure history.

216



217

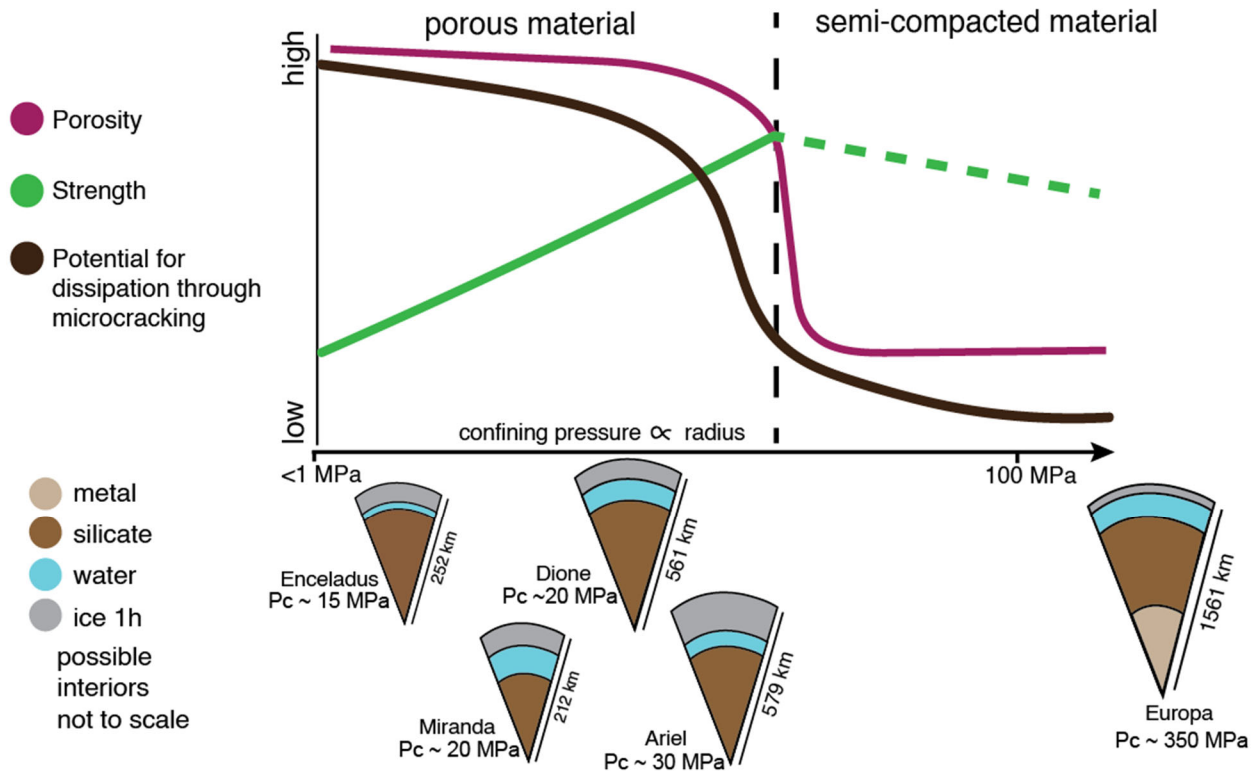
218 Figure 3: Results from ultrasonic pulsing during confining pressure oscillation. a) V_p wavespeeds. b) V_s
 219 wavespeeds. c) V_p/V_s ratio. For a-c, linear trendlines are shown in black, with grey lines denoting 90%
 220 confidence interval. d) Two full depressurization-repressurization cycles and resultant waveforms. Black
 221 line indicates pressure conditions. Waveforms are stacked with increasing experimental time, and color
 222 corresponds with amplitude over wavelength time, from blue (high negative amplitude) to brown (high
 223 positive amplitude). Horizontal, discontinuous lines marked with stars are energetic acoustic emission
 224 events, which are separate from the pulsed ultrasonic waves shown here. e) Sample waveforms from 0
 225 and 50 MPa confining pressure at each inflection point in the cycle. Similar parts of the waveform at 0
 226 and 50 MPa are highlighted in light grey boxes. See Supplementary Information for further discussion of
 227 waveform analysis (S4-6).

228

229 **4. Discussion**

230

231



232

233 Figure 4: A conceptual diagram showing the effects of confining pressure on porosity, strength, and the
 234 power released via microcracking. Sample interior models for small icy moons are shown in order of
 235 increasing P_c at the ocean-rock interface, based on estimates from PlanetProfile by Vance et al (2018).

236 The above results show that the mechanical and acoustic properties of chondritic material, and therefore
 237 the cores of icy moons, are dependent on confining pressure. Several of these relationships are depicted
 238 schematically in Figure 4.

239 4.1. Discussion of mechanical data

240 Chondritic material initially strengthens with increasing confining pressure, then undergoes a drop in peak
 241 differential stress above confining pressures $>50\text{ MPa}$ (Figure 1a, 1c). This behavior is similar to the “cap
 242 model” for compaction and deformation of porous Earth materials. In the cap model porosity drops
 243 steadily with increasing pressure before dropping rapidly at a point of compactive yield (C^*), where the
 244 load-bearing framework collapses and above which cataclastic flow takes over as the primary mode of
 245 deformation (Wong and Baud, 2012).

246 Pore closure may therefore proceed in a predictable, yet discontinuous manner across icy moon
 247 environments. The maximum pressure at which porosity is maintained within a rocky interior should
 248 decrease with increasing P_c , then suddenly drop, rather than a slow closure similar to that within the outer
 249 layers of rocky planets as is often assumed in planetary models (e.g. Vance et al., 2018). The pores do not
 250 close entirely at this point, but most porosity is lost. It is possible that the maximum normal stress seen in
 251 our test, 350 MPa, represents the condition for total pore closure. Assumptions of density and
 252 permeability within cores should see a similar jump. These observations indicate that the mechanisms of

253 deformation may be different in larger moons than in smaller moons, due to the increased confining
254 pressures from increased overburden at the rock-ocean or rock-ice interface. In bodies where rocky
255 interiors are under higher confining pressures, pore closure effects may not be as important and material
256 may be stiffer; in lower-pressure environments, material may deform more easily.

257 Viscoelastic deformation of silicate interiors has been suggested as a mechanism for heat generation and
258 tidal dissipation in Enceladus and Europa (Kang et al., 2020; Liao et al., 2020; Rovira-Navarro et al.,
259 2022), but a true viscous response is unlikely in a cold, chondritic layer. Silicates typically require
260 elevated pressures and temperatures for viscous deformation (e.g. Kohlstedt and Hansen, 2015). Brittle
261 creep, a mechanism that is active in silicate rocks at low pressures and temperatures (Bernabé and Peč,
262 2022; Brantut et al., 2013) may generate an additional apparent viscous response, contributing to the total
263 heat dissipation via microcracking. Similar effects may arise from pore closure and reopening. While not
264 truly a viscous response, the presence of brittle creep could serve as a nonlinear viscous element over
265 short timescales and thus should be considered in models for viscoelastic core deformation.

266

267 **4.2. Discussion of acoustic and ultrasonic data**

268 Dissipative acoustic emissions from microcracking events occurred at all pressures sampled, even
269 at low differential stresses, indicating that even small changes to local stresses can initiate cracks (Figure
270 2). The V_p/V_s ratio also decreased with increasing confining pressure (Figure 3c), which occurs as
271 damage increases (Wang et al., 2012). We suggest that microcracking could be continuously occurring in
272 rocky interiors of icy satellites, where deviatoric stresses can be on the order of 1 MPa or higher,
273 changing periodically with the orbit of the satellite (Gao and Stevenson, 2013; McKinnon, 2013). As
274 these cracks occurred during the nominally elastic component of deformation (low differential stress, low
275 strain; see Figure 2b, 2e), we suggest that that the energy from these microscale plastic mechanisms
276 should be associated with the apparent viscous response necessary for dissipation in the silicate core.

277 Moons with thinner crusts and oceans could receive proportionally more heat over their lifetimes
278 from the deformation of their rocky interiors than larger moons, as their cores will be more deformable at
279 low pressures and therefore able to dissipate heat during viscoelastic deformation. Local values of σ_1 will
280 be lower in smaller moons as well, corresponding to the most energetic cracking events seen in our tests
281 (Figure 2c, 2f). As this energy is released, it could contribute to processes such as ice overturn, ocean
282 maintenance, and possibly even geyser activity as seen on Enceladus' south pole. Pore fluids change the
283 local stress state by lowering the effective pressure, so that materials at the ocean-silicate interface could
284 experience even more fracture than we observe in lab. Additionally, while our deformation experiments
285 are conducted at relatively slow strain rates, they are not identical to timescales and frequencies of tidal
286 deformation. Under realistic tidal forcing periods, the strength of porous rocks is lower (Bagde and
287 Petroš, 2009; Peng et al., 2020), increasing the likelihood of cracking in response to small stress changes.
288 One excellent opportunity for future laboratory studies is the measurement of acoustic properties of
289 aqueously altered chondritic material, which should exist at the rock-ocean boundary.

290 In addition to releasing heat at the time of their formation, cracks create new surface area. Modeling
291 by Rovira-Navarro et al. (2022) found that rock-water interaction (via increasing permeability) increases
292 dissipation throughout a porous core. Fresh surface area would encourage serpentinization, which has
293 been suggested as a mechanism for generating hydrogen within the oceans of icy bodies (Kamata et al.,

294 2019; McCollom et al., 2022; Neveu et al., 2015; Vance and Melwani Daswani, 2020) or cultivation of
295 organic materials which have risen to Titan's surface (Castillo-Rogez and Lunine, 2010). Many of these
296 reactions include volume increase which modifies the local stress field, encouraging further cracking
297 within the silicate body and providing a self-sustaining heating process.

298

299 5. Conclusions

300 We characterized the mechanical properties of stony chondritic material under a range of confining
301 pressures, defined a failure envelope, measured wavespeeds, and retrieved both static and dynamic elastic
302 moduli. The mechanical results suggest that porosity decreases significantly at lab confining pressure of
303 ~50 MPa, such that the silicate interiors of larger icy moons will be relatively dense and impermeable.
304 The interiors of larger moons are less deformable, and therefore contribute proportionally less energy in
305 response to tidal forcing, than those of smaller moons. We also observed semi-continuous energy release
306 arising from microcracking under small changes to stress. These microcracks may represent an apparent
307 viscous response which enhances heat dissipation within rocky cores and mantles. The energy release
308 from microcracking occurred during pressurization and depressurization as well, and transmissivity of the
309 material (likely dependent on its porosity) was a function of current confining pressure rather than
310 pressure history. Pressure, and the resultant amount of porosity that a material can maintain, is therefore a
311 strong control on the dissipative potential of silicate interiors. These findings are useful for determining
312 the level of heat generated in the cores and mantles of icy moons, which may then drive ocean circulation
313 and/or maintenance. We also see that the release of energy persists as deformation continues, indicating
314 that ongoing deformation on a diurnal timescale may remain important for the total heat flux of an icy
315 body.

316

317

318 **Acknowledgements:** CS received support from Massachusetts Space Grant fellowship and MathWorks.
319 Figures were plotted using perceptually uniform colormaps from Crameri (2021). CORd laboratory
320 technician support by NSF grant # 2054414 is gratefully acknowledged. Thank you to Veronique LeRoux
321 for CT scans, Mark Panning, Mohit Melwani Deswani, and Laurent Pou for discussions on icy moon
322 interiors, and to Rick Binzel for early input on the project.

323

324 **Data Availability Statement:** All mechanical, ultrasonic, and acoustic data can be found at
325 <https://zenodo.org/records/10211457> (Seltzer, 2023).

326

327 Aygün, B., Čadek, O., 2022. A new approach to modeling the tidal dissipation in subsurface oceans of icy
328 moons of Jupiter and Saturn (other). oral. <https://doi.org/10.5194/epsc2022-968>
329 Bagde, M.N., Petroš, V., 2009. Fatigue and dynamic energy behaviour of rock subjected to cyclical
330 loading. *International Journal of Rock Mechanics and Mining Sciences* 46, 200–209.
331 <https://doi.org/10.1016/j.ijrmms.2008.05.002>

- 332 Bernabé, Y., Peč, M., 2022. Brittle Creep and Failure: A Reformulation of the Wing Crack Model.
333 *Journal of Geophysical Research: Solid Earth* 127, e2022JB024610.
334 <https://doi.org/10.1029/2022JB024610>
- 335 Brantut, N., Heap, M.J., Meredith, P.G., Baud, P., 2013. Time-dependent cracking and brittle creep in
336 crustal rocks: A review. *Journal of Structural Geology* 52, 17–43.
337 <https://doi.org/10.1016/j.jsg.2013.03.007>
- 338 Castillo-Rogez, J.C., Lunine, J.I., 2010. Evolution of Titan's rocky core constrained by Cassini
339 observations. *Geophysical Research Letters* 37. <https://doi.org/10.1029/2010GL044398>
- 340 Cramer, F., 2021. Scientific colour maps. <https://doi.org/10.5281/zenodo.5501399>
- 341 Eitzen, D.G., Wadley, H.N.G., 1984. Acoustic Emission: Establishing the Fundamentals. *J. RES. NATL.*
342 *BUR. STAN.* 89, 75. <https://doi.org/10.6028/jres.089.008>
- 343 Flynn, G.J., Consolmagno, G.J., Brown, P., Macke, R.J., 2018. Physical properties of the stone
344 meteorites: Implications for the properties of their parent bodies. *Geochemistry* 78, 269–298.
345 <https://doi.org/10.1016/j.chemer.2017.04.002>
- 346 Gao, P., Stevenson, D.J., 2013. Nonhydrostatic effects and the determination of icy satellites' moment of
347 inertia. *Icarus* 226, 1185–1191. <https://doi.org/10.1016/j.icarus.2013.07.034>
- 348 Ghaffari, H.O., Mok, U., Pec, M., 2021. On calibration of piezoelectric sensors with laser doppler
349 vibrometer. *The Journal of the Acoustical Society of America* 150, 2503–2513.
350 <https://doi.org/10.1121/10.0006445>
- 351 Ghaffari, H.O., Nasser, M.H.B., Young, R.P., 2014. Faulting of Rocks in a Three-Dimensional Stress
352 Field by Micro-Anticracks. *Sci Rep* 4, 5011. <https://doi.org/10.1038/srep05011>
- 353 Hogan, J.D., Kimberley, J., Hazeli, K., Plescia, J., Ramesh, K.T., 2015. Dynamic behavior of an ordinary
354 chondrite: The effects of microstructure on strength, failure and fragmentation. *Icarus* 260, 308–
355 319. <https://doi.org/10.1016/j.icarus.2015.07.027>
- 356 Jackson, I., 2015. Properties of Rocks and Minerals: Physical Origins of Anelasticity and Attenuation in
357 Rock, in: *Treatise on Geophysics*. Elsevier, pp. 539–571. <https://doi.org/10.1016/B978-0-444-53802-4.00045-2>
- 358
- 359 Kamata, S., Nimmo, F., Sekine, Y., Kuramoto, K., Noguchi, N., Kimura, J., Tani, A., 2019. Pluto's ocean
360 is capped and insulated by gas hydrates. *Nat. Geosci.* 12, 407–410.
361 <https://doi.org/10.1038/s41561-019-0369-8>
- 362 Kang, W., Bire, S., Campin, J.-M., Sotin, C., German, C., Thurnherr, A., Marshall, J., 2020. Differing
363 Enceladean ocean circulation and ice shell geometries driven by tidal heating in the ice versus the
364 core.
- 365 Kimberley, J., Ramesh, K.T., 2011. The dynamic strength of an ordinary chondrite. *Meteoritics &*
366 *Planetary Science* 46, 1653–1669. <https://doi.org/10.1111/j.1945-5100.2011.01254.x>
- 367 Kohlstedt, D.L., Hansen, L.N., 2015. Constitutive Equations, Rheological Behavior, and Viscosity of
368 Rocks, in: *Treatise on Geophysics*. Elsevier, pp. 441–472. <https://doi.org/10.1016/B978-0-444-53802-4.00042-7>
- 369
- 370 Kuskov, O.L., Kronrod, V.A., 2005. Internal structure of Europa and Callisto. *Icarus*, Europa Icy Shell
371 177, 550–569. <https://doi.org/10.1016/j.icarus.2005.04.014>
- 372 Lei, X., Ma, S., 2014. Laboratory acoustic emission study for earthquake generation process. *Earthq Sci*
373 27, 627–646. <https://doi.org/10.1007/s11589-014-0103-y>
- 374 Li, X., Si, G., Oh, J., Canbulat, I., Xiang, Z., Zhang, X., 2021. Laboratory characterisation of anisotropic
375 and heterogeneous damage of rock sample using acoustic emission and ultrasonic monitoring
376 technologies. *IOP Conf. Ser.: Earth Environ. Sci.* 861, 022040. <https://doi.org/10.1088/1755-1315/861/2/022040>
- 377
- 378 Liao, Y., Nimmo, F., Neufeld, J.A., 2020. Heat Production and Tidally Driven Fluid Flow in the
379 Permeable Core of Enceladus. *Journal of Geophysical Research: Planets* 125, e2019JE006209.
380 <https://doi.org/10.1029/2019JE006209>

- 381 Mair, K., Elphick, S., Main, I., 2002. Influence of confining pressure on the mechanical and structural
382 evolution of laboratory deformation bands. *Geophysical Research Letters* 29, 49-1-49-4.
383 <https://doi.org/10.1029/2001GL013964>
- 384 McCollom, T.M., Klein, F., Ramba, M., 2022. Hydrogen generation from serpentinization of iron-rich
385 olivine on Mars, icy moons, and other planetary bodies. *Icarus* 372, 114754.
386 <https://doi.org/10.1016/j.icarus.2021.114754>
- 387 McKinnon, W.B., 2013. The shape of Enceladus as explained by an irregular core: Implications for
388 gravity, libration, and survival of its subsurface ocean. *Journal of Geophysical Research: Planets*
389 118, 1775–1788. <https://doi.org/10.1002/jgre.20122>
- 390 Mulliken, A.D., Boyce, M.C., 2006. Mechanics of the rate-dependent elastic–plastic deformation of
391 glassy polymers from low to high strain rates. *International Journal of Solids and Structures* 43,
392 1331–1356. <https://doi.org/10.1016/j.ijsolstr.2005.04.016>
- 393 Néri, A., Guyot, F., Reynard, B., Sotin, C., 2020. A carbonaceous chondrite and cometary origin for icy
394 moons of Jupiter and Saturn. *Earth and Planetary Science Letters* 530, 115920.
395 <https://doi.org/10.1016/j.epsl.2019.115920>
- 396 Neumann, W., Kruse, A., 2019. Differentiation of Enceladus and Retention of a Porous Core. *ApJ* 882,
397 47. <https://doi.org/10.3847/1538-4357/ab2fcf>
- 398 Neveu, M., Desch, S.J., Castillo-Rogez, J.C., 2015. Core cracking and hydrothermal circulation can
399 profoundly affect Ceres’ geophysical evolution. *Journal of Geophysical Research: Planets* 120,
400 123–154. <https://doi.org/10.1002/2014JE004714>
- 401 Nimmo, F., Pappalardo, R.T., 2016. Ocean worlds in the outer solar system. *Journal of Geophysical*
402 *Research: Planets* 121, 1378–1399. <https://doi.org/10.1002/2016JE005081>
- 403 O’Ghaffari, H., Peč, M., Mittal, T., Mok, U., Chang, H., Evans, B., 2023. Microscopic defect dynamics
404 during a brittle-to-ductile transition. *Proceedings of the National Academy of Sciences* 120,
405 e2305667120. <https://doi.org/10.1073/pnas.2305667120>
- 406 Paterson, M.S., 1990. Rock Deformation Experimentation, in: *The Brittle-Ductile Transition in Rocks*.
407 American Geophysical Union (AGU), pp. 187–194. <https://doi.org/10.1029/GM056p0187>
- 408 Peng, K., Zhou, J., Zou, Q., Song, X., 2020. Effect of loading frequency on the deformation behaviours of
409 sandstones subjected to cyclic loads and its underlying mechanism. *International Journal of*
410 *Fatigue* 131, 105349. <https://doi.org/10.1016/j.ijfatigue.2019.105349>
- 411 Pohl, L., Britt, D.T., 2020. Strengths of meteorites—An overview and analysis of available data.
412 *Meteoritics & Planetary Science* 55, 962–987. <https://doi.org/10.1111/maps.13449>
- 413 Ramesh, K.T., Stickle, A.M., Kimberley, J., 2017. Rocks, Shocks and Asteroids, and Some Interesting
414 Research Directions in Mechanics: 2015 Murray Lecture Paper. *Experimental Mechanics* 57,
415 1149–1159. <https://doi.org/10.1007/s11340-017-0324-9>
- 416 Rovira-Navarro, M., Katz, R.F., Liao, Y., van der Wal, W., Nimmo, F., 2022. The Tides of Enceladus’
417 Porous Core. *Journal of Geophysical Research: Planets* 127, e2021JE007117.
418 <https://doi.org/10.1029/2021JE007117>
- 419 Seltzer, C., 2023. Supporting data for “Mechanical properties of the rocky interiors of icy moons”
420 [DATASET]. <https://doi.org/10.5281/zenodo.10211457>
- 421 Styczinski, M.J., Vance, S.D., Melwani Daswani, M., 2022. PlanetProfile: Self-consistent interior
422 structure modeling for terrestrial bodies in Python (preprint). *Planetology*.
423 <https://doi.org/10.1002/essoar.10512890.1>
- 424 Tobie, G., Mocquet, A., Sotin, C., 2005. Tidal dissipation within large icy satellites: Applications to
425 Europa and Titan. *Icarus, Europa Icy Shell* 177, 534–549.
426 <https://doi.org/10.1016/j.icarus.2005.04.006>
- 427 Vance, S.D., Melwani Daswani, M., 2020. Serpentine and the search for life beyond Earth.
428 *Philosophical Transactions of the Royal Society A: Mathematical, Physical and Engineering*
429 *Sciences* 378, 20180421. <https://doi.org/10.1098/rsta.2018.0421>
- 430 Vance, S.D., Panning, M.P., Stähler, S., Cammarano, F., Bills, B.G., Tobie, G., Kamata, S., Kedar, S.,
431 Sotin, C., Pike, W.T., Lorenz, R., Huang, H.-H., Jackson, J.M., Banerdt, B., 2018. Geophysical

- 432 Investigations of Habitability in Ice-Covered Ocean Worlds. *Journal of Geophysical Research:*
433 *Planets* 123, 180–205. <https://doi.org/10.1002/2017JE005341>
- 434 Voropaev, S.A., Kocherov, A.V., Lorenz, C.A., Korochantsev, A.V., Dushenko, N.V., Kuzina, D.M.,
435 Nugmanov, I.I., Jianguo, Y., 2017. Features in constructing a certificate of strength of
436 extraterrestrial material by the example of the Chelyabinsk meteorite. *Dokl. Phys.* 62, 486–489.
437 <https://doi.org/10.1134/S1028335817100111>
- 438 Voropaev, S.A., Nugmanov, I.I., Dushenko, N.V., Jianguo, Y., 2020. Dependence of the Elastic
439 Properties of H5-Chondrites (NWA 12370) on Pressure. *Dokl. Phys.* 65, 383–386.
440 <https://doi.org/10.1134/S1028335820110105>
- 441 Wang, X.-Q., Schubnel, A., Fortin, J., David, E.C., Guéguen, Y., Ge, H.-K., 2012. High V_p/V_s ratio:
442 Saturated cracks or anisotropy effects? *Geophysical Research Letters* 39.
443 <https://doi.org/10.1029/2012GL051742>
444
- 445